

# **Impact of imposed drying on deep convection in a cloud-resolving model**

S. Wang,<sup>1</sup> and A. H. Sobel<sup>2</sup>

-----

Shuguang Wang, Department of Applied Physics and Applied Mathematics,  
Columbia University, New York, New York 10027 (sw2526@columbia.edu)

Adam H. Sobel, Department of Applied Physics and Applied Mathematics,  
Department of Earth and Environmental Sciences, Lamont-Doherty Earth  
Observatory, Columbia University, New York, New York 10027

<sup>1</sup> Department of Applied Physics and Applied  
Mathematics, Columbia University,  
New York, New York 10027, USA

<sup>2</sup> Department of Applied Physics and Applied  
Mathematics, Department of Earth and  
Environmental Sciences, and Lamont-Doherty  
Earth Observatory, Columbia University,  
New York, New York 10027, USA.

Submitted to Journal of Geophysical Research – Atmosphere for Publication  
September 2011

## Abstract

1           This study uses a cloud-resolving model under the weak temperature gradient (WTG)  
2 approximation to explore the response of deep convection to imposed drying. The drying,  
3 intended to mimic horizontal advection of dry air, is imposed as a linear relaxation of the  
4 humidity field towards zero within a specified layer. Radiative cooling and sea surface  
5 temperature are held constant and there is no mean vertical shear in the integrations. The  
6 statistically steady responses to drying in the lower, middle, and upper free troposphere are  
7 compared.

8           The rain rate decreases with drying when that drying is imposed in the lower or middle  
9 free troposphere, more strongly so for lower tropospheric drying. The decrease in rainfall is  
10 linearly proportional to the drying to a good approximation. Upper-tropospheric drying has  
11 almost no impact on the rain rate. For lower-tropospheric drying, the decrease in rain rate with  
12 drying can be well explained by assuming that both an appropriately defined normalized gross  
13 moist stability and surface turbulent fluxes remain constant as drying varies. For middle- and  
14 upper-tropospheric drying, the normalized gross moist stability decreases with drying, allowing  
15 the precipitation to decrease less rapidly or not at all. The variations in normalized gross moist  
16 stability in turn result from changes in the large-scale vertical motion profiles. These are  
17 predominantly top-heavy, becoming somewhat less so with small or moderate drying. Over most  
18 of the range of drying strengths, the changes to the shape of the vertical motion profile are  
19 greatest for upper-tropospheric drying and smallest for lower-tropospheric drying. For very  
20 strong lower-tropospheric drying, however, the vertical motion profile becomes bottom-heavy  
21 and the normalized gross moist stability becomes negative.

## 22 1. Introduction

23 Atmospheric moist convection plays critical roles in regulating tropical circulations on a  
24 wide spectrum of temporal and spatial scales, ranging from high impact weather, to intra-  
25 seasonal variability, to large scale overturning circulations. Yet our understanding of tropical  
26 convection's interaction with larger scales is limited, particularly as that understanding is  
27 expressed by convective parameterizations in climate models. Incorrect sensitivity of  
28 parameterized convection to environmental humidity has become widely recognized as a critical  
29 factor limiting model performance [e.g., *Derbyshire et al.*, 2004]. In nature, convection and  
30 humidity interact in a complex fashion. The causal link between humidity and convection is  
31 often difficult to disentangle. A more humid free troposphere may cause stronger convection but  
32 may also be in part a consequence of convective transport. In this study, we probe humidity-  
33 convection interaction by studying the impact of imposed drying on statistically steady moist  
34 convection using a cloud resolving model.

35 Several studies have explored the impact of moisture perturbations on convection, either  
36 using single column models with parameterized convection [e.g., *Derbyshire et al.*, 2004; *Sobel*  
37 *and Bellon*, 2009, hereafter SB09], or cloud-resolving models (CRMs) with explicitly resolved  
38 convection [e.g., *Takemi et al.*, 2004; *Kuang*, 2010; *Tulich and Mapes*, 2010; *James and*  
39 *Markowski*, 2010]. Using the weak temperature gradient approximation, SB09 explored the  
40 impact of imposed drying in specified vertical layers on parameterized convection interacting  
41 with large scale dynamics. They found that drying in the middle layer was more effective than  
42 drying in the lower layer in suppressing deep convection, in both of two very different single  
43 column models (SCMs). On the other hand, studies using cloud-resolving models by *Tulich and*  
44 *Mapes* [2010] and *Kuang* [2010] both showed that sensitivity to moisture perturbations in the

45 lower troposphere was greater than to those in the middle or upper troposphere. SB09 suggested  
46 that the weaker response to lower-tropospheric drying in their results might be due to inadequate  
47 sensitivity of parameterized convection to lower-tropospheric moisture, and that it would be  
48 highly desirable to conduct similar experiments with a cloud resolving model.

49         In this study, following SB09, we continue to explore convective responses to external  
50 humidity forcing with a cloud-resolving model under the weak temperature gradient (WTG)  
51 approximation. Under WTG, large-scale vertical motion is parameterized, allowing interaction  
52 between convection and the large-scale divergent circulation without explicit simulation of the  
53 latter using the equations of motion on a large domain. With this method, not only the amplitude  
54 but also the vertical structure of the large-scale vertical motion is determined internally as part of  
55 the solution. Several studies using WTG have found that the parameterized vertical motion is  
56 top-heavy in deep convective conditions [e.g., *Sobel and Bretherton, 2000; Raymond and Zeng,*  
57 *2005; Kuang, 2011; Wang and Sobel, 2011*], although the degree of top-heaviness may be  
58 sensitive to the details of either the implementation of WTG or the model physics. A notable  
59 exception is the study by *Raymond and Sessions [2007]*. They performed WTG CRM  
60 simulations in which warming in the upper free troposphere and cooling below were added to a  
61 reference temperature profile derived from a radiative-convective equilibrium simulation, and  
62 found that the increased gravitational stability led to bottom-heavy mass flux profiles.

63         In nature, both bottom- and top-heavy vertical motion profiles have been observed. In  
64 the tropics, because WTG balance holds approximately, the vertical motion profile tends to be  
65 similar to the diabatic heating profile, which has long been known to have its maximum at  
66 different levels in different geographic regions [e.g., *Webster and Lukas, 1992*]. *Back and*  
67 *Bretherton [2006]* demonstrated that, in both reanalysis data and climate models, top-heavy

68 profiles are common in the west Pacific warm pool region, while bottom-heavy profiles are more  
69 typical in the east Pacific ITCZ region. *Yuan and Hartmann* [2008] further demonstrated that,  
70 over a large range of time scales from several hours to months, the “top-heaviness” of vertical  
71 motions is consistent with the penetration depth of cloud systems.

72         The degree of bottom- or top-heaviness of the large-scale vertical motion profile is  
73 important to the moist static energy (or moist entropy) budget, as it strongly influences the  
74 vertical advection of moist static energy and the associated gross moist stability [*Neelin*, 1997;  
75 *Back and Bretherton*, 2006; *Sobel*, 2007; *Frierson*, 2007; *Frierson et al.*, 2011]. The most  
76 important dynamical factors leading to the occurrence of bottom-heavy vertical motion profiles  
77 are unclear at present. One may interpret bottom-heavy ascent as the ascending branch of a  
78 shallow meridional overturning circulation [*Zhang et al.*, 2008; *Nolan et al.*, 2007, 2010]. In the  
79 east Pacific, one argument [*Sobel*, 2007] is that results from a local SST maximum with large  
80 gradients around it, leading to large surface convergence by the Lindzen-Nigam mechanism  
81 [*Lindzen and Nigam*, 1987], yet which is not as warm as the warmest tropical oceans globally or  
82 even regionally, resulting in only modest instability of the local profile to deep convection. An  
83 additional factor, suggested by both theoretical and observational studies [*Sobel and Neelin*,  
84 2006, *Peters et al.*, 2008] is that transient eddies (with time scales of days) may transport dry air  
85 into ITCZ regions, limiting the penetration depth of convection through entrainment processes.  
86 The importance of dry air intrusions has also been recognized in several case studies [e.g., *Brown*  
87 *and Zhang*, 1997; *Lucas and Zipser*, 2000; *Redelsperger et al.*, 2002; *Roca et al.*, 2005; *Zuidema*  
88 *et al.*, 2006; *Allen et al.*, 2009]. On the other hand, the hypothesis that drying may induce  
89 bottom-heavy profiles was not supported by the results of SB09 using parameterized convection.

90 Here, we further explore this drying hypothesis using CRM, and demonstrate that drying can  
91 indeed suppress deep convection and lead to bottom heavy vertical motion.

92 In Section 2, we present our numerical experiment design. This closely follows SB09,  
93 apart from differences resulting from the inherent differences between SCMs and CRMs. A  
94 cloud-resolving model, documented in detail in *Wang and Sobel* [2011], is used to study  
95 convective response to the imposed drying. Results are presented in Section 3. Section 4 contains  
96 discussion and conclusions.

## 97 **2. Numerical model and experiment design**

### 98 **2.1. Numerical model**

99 We use the Advanced Research Weather Research and Forecasting (WRF) Model version  
100 3.0 [*Skamarock et al.*, 2008]. We have configured WRF to run under either the WTG or  
101 radiative-convective equilibrium (RCE) mode. Use of WTG allows two-way interaction between  
102 the explicitly simulated convection and a parameterized large scale vertical motion field. Details  
103 of our implementation of WTG have been documented in *Wang and Sobel* [2011]; the primary  
104 difference from that used in SCM studies such as SB09 (but similar to other CRM studies, e.g.,  
105 *Raymond and Zeng* [2005], *Raymond and Sessions* [2007], *Sessions et al.* [2010]) is that the  
106 horizontal mean temperature field in the free troposphere is not strictly held to a prescribed  
107 profile, but relaxed towards it on a specified time scale, here taken to be three hours. We adopt  
108 the following physics schemes: boundary layer turbulence and vertical subgrid eddies are  
109 parameterized using the Yonsei University (YSU) scheme; horizontal subgrid eddies are treated  
110 using Smagorinsky first order closure; the surface moisture and heat fluxes are parameterized  
111 following the Monin-Obukhov similarity theory; the Purdue-Lin scheme is used for cloud  
112 microphysics, and simplified radiative cooling (constant 1.5 K/day cooling in the troposphere) is

113 applied in place of interactive radiation. The horizontal and vertical advection schemes are 5<sup>th</sup>  
114 order and 3<sup>rd</sup> order accurate, respectively. Moisture and other scalars are advected using a  
115 positive definite scheme [Skamarock *et al.*, 2008]. We use the implicit scheme [Klemp *et al.*,  
116 2009] to damp unphysical reflection of vertically propagating gravity waves in the top 5 km of  
117 the numerical grid. These schemes (except the constant radiative cooling) are commonly used for  
118 numerical weather prediction.

119 All the numerical experiments were performed with horizontal grid spacing of 2 km and  
120 constant Coriolis parameter  $f=0$ . We use 50 vertical levels with 10 levels in the lowest 1 km and  
121 grid spacing gradually increasing to 1.5 km near the model top  $\sim 22$  km. The computational  
122 domain has 96x96 horizontal grid points and doubly periodic lateral boundary conditions.

## 123 **2.2 Numerical Experiments**

124 To facilitate the comparison between convection in our cloud resolving model and  
125 parameterized convection in the single column models in SB09, we closely follow their strategy  
126 to design the numerical experiments.

127 We first use the RCE solution, computed over an SST of 28°C, to derive the target  
128 temperature profile for the WTG integrations. The WTG integrations are then carried out over  
129 an SST of 30°C, 2°C higher than that over which the RCE was obtained. Without any imposed  
130 drying, the WTG equilibrium is quite rainy because the relatively high SST leads to high local  
131 instability. The solution in this case is identical to the three-dimensional WTG experiment with  
132 SST = 30°C in *Wang and Sobel* [2011]. The rain rate in this case is  $\sim 22$  mm/day, much higher  
133 than the RCE rain rate at SST = 28°C ( $\sim 4.5$  mm/day). The WTG vertical velocity is top-heavy,  
134 with a maximum value of  $\sim 11$  cm/s in the upper troposphere. *Wang and Sobel* [2011] showed  
135 that this top-heavy profile is remarkably self-similar as SST varies above the RCE value (28°C),

136 retaining an almost identical shape and varying only in amplitude. Both the top-heavy WTG  
 137 vertical velocity and cloud mass flux indicate the dominance of deep convection at SST=30°C.  
 138 Here, with SST held constant at 30°C, we carry out a set of integrations in which we impose  
 139 drying with varying strength to isolate the impact of drying on the equilibrated solution.

140 Drying is imposed as a relaxation of the domain averaged water vapor mixing to zero in  
 141 the tendency equation of moisture:

$$142 \quad \frac{\partial Q_v}{\partial t} + \dots = -\frac{[Q_v]}{\tau_q} \quad \text{for } \eta_1 < \eta < \eta_2 \quad (1),$$

143 where  $Q_v$  is the mixing ratio of water vapor,  $\tau_q$  is the time scale for the imposed drying, and  $[\ ]$   
 144 denotes the domain average. The relaxation is applied only where the dry mass  $\eta$  (the WRF  
 145 vertical coordinate) falls between  $\eta_1$  and  $\eta_2$ . As in SB09, we impose drying in three different  
 146 vertical layers in three sets of simulations. We refer to these as the lower, middle, and upper  
 147 troposphere, corresponding to three ranges in  $\eta$ : (0.6, 0.825), (0.375, 0.6) and (0.150, 0.375),  
 148 respectively. These three layers are nearly identical to the three pressure ranges: 600-825 hPa,  
 149 375-600 hPa, 150-375 hPa in SB09.

150 The drying time scale,  $\tau_q$ , is the control parameter that is varied in each of the three sets  
 151 of experiments, as shown in Table 1. It is useful to express the results not only in terms of  $\tau_q$ ,  
 152 but also in terms of the vertically integrated energy removal due to the drying,  $F_q$ :

$$153 \quad F_q = \frac{1}{\tau_q} \int_{\eta_1}^{\eta_2} L Q_v \frac{\mu d\eta}{g} \quad (2),$$

154 where  $g$  is gravity,  $p$  is the pressure, and  $\mu$  is the total dry mass.

155 The drying time scale cannot approach zero for numerical reasons, as discussed in SB09.  
156 In this model, further drying (smaller  $\tau_q$ ) than the minimum values for  $\tau_q$  shown here would  
157 produce negative moisture. As large amplitude forcing (e.g., comparable to or greater than the  
158 sum of surface fluxes and radiative cooling) is used in many of the integrations, we are not  
159 necessarily in the regime of small amplitude perturbations as in *Tulich and Mapes* [2010] and  
160 *Kuang* [2010]. As will be shown below, however, even with large moisture perturbations  
161 (strengthening to its limit), linearity can hold remarkably well.

162 All the numerical experiments are integrated for 25 days. The last 15 days are averaged to  
163 obtain the statistically steady state, unless otherwise mentioned.

### 164 **3. Results**

#### 165 **3.1 Precipitation as a function of imposed drying**

166 Figure 1 shows daily mean precipitation ( $P$  in mm/day) versus drying time scale  $\tau_q$   
167 (Panel a) and energy export  $F_q$  (Panel b).  $P$  decreases with respect to either increased energy  
168 export or decreased drying time scale. For lower layer drying,  $P$  is reduced from  $\sim 22$  mm/day  
169 with zero drying to  $\sim 4$  mm/day with  $\tau_q = 70$  hours (lowest value of  $\tau_q$ ). With a modest time  
170 scale ( $\tau_q > 10$  days)  $P$  remains high for the middle layer drying case. With a further decrease in  
171  $\tau_q$  to 30 hours or an increase in  $F_q$  to  $110 \text{ W/m}^2$ , drying in the middle layer is able to reduce  
172 rainfall to 15 mm/day. On the other hand, drying in the upper layer seems to have little impact on  
173 precipitation.  $P$  remains above 20 mm/day in this case even when energy export exceeds 50  
174  $\text{W/m}^2$ ; for the same amount of energy export, precipitation is substantially reduced in the other  
175 cases. This suggests that moisture at upper levels is mainly a result of convection rather than  
176 having a strong causal influence on convection, as suggested by observational studies [*Sherwood,*

177 1999; *Sherwood and Wahrlich*, 1999; *Straub and Kiladis* 2002, 2003; *Sobel et al.* 2004].  
178 However, an interesting aspect is that precipitation is slightly increased by  $\sim 1$  mm/day in the  
179 upper layer drying experiments with  $\tau_q$  less than 1 day ( $F_q > 20$  W/ m<sup>2</sup>). Limited examination by  
180 sub-sampling the latter time period of the integrations (when the rain rate is quasi-steady)  
181 suggest that this is not a result of sampling error, although longer integrations would be needed  
182 to be certain of this. It has been proposed, for example, that drying can promote convection,  
183 because overlaying of dry layers upon moist layers creates potential instability [*Allen et al.*,  
184 2009]; more analysis would be needed to determine if our results support this idea.

185 The  $P$  versus  $F_q$  relationship is remarkably linear. Let  $\Delta P = -\alpha \cdot F_q$ , where  $\alpha$  is an  
186 empirical linear slope. If  $P$  is expressed using energy unit in W/m<sup>2</sup>, using a constant of (28.9 W/  
187 m<sup>2</sup>)/(1 mm/day), the non-dimensional slope  $\alpha$  is 3.1, 1.9, and -0.4 for lower, middle and upper  
188 layer drying, respectively. The value of  $\alpha=3.1$  for lower layer drying is nearly equal to the  
189 inverse of normalized gross moist stability, as discussed in Section 3.5.

190 At a given drying time scale or energy export, lower layer drying most efficiently  
191 suppresses convection compared with middle or upper layer drying. This result is consistent with  
192 other modeling studies [*Tulich and Mapes*, 2010; *Kuang* 2010]. Presumably because moisture at  
193 upper levels responds more or less passively to convection and large-scale ascent, drying at  
194 upper levels has little impact.

195 Figure 1b also shows surface fluxes (the sum of latent heat  $E$  and sensible flux  $H$ ), versus  
196  $F_q$  for all experiments. In contrast to precipitation, surface fluxes vary little with  $F_q$ . For example,  
197  $P$  decreases to the RCE value (4.8mm/day) for large values of lower layer drying, but surface  
198 fluxes only decrease by less than 2 mm/day over this range, and remain much greater than the  
199 RCE value. Precipitation  $P$  and total turbulent surface flux  $E+H$  are positively correlated. It

200 should be kept in mind that these simulations do not include either ocean coupling or cloud-  
201 radiative feedback. These effects could qualitatively change the relationship of the total  
202 turbulent surface flux  $E+H$  to precipitation, though without necessarily changing the sum of that  
203 and vertically integrated radiative cooling, which is the total forcing of the moist static energy  
204 budget by diabatic processes [Sobel, 2003].

205 In addition, Figure 1b shows the sum of surface fluxes and vertically-integrated radiative  
206 cooling; this is the total diabatic forcing of vertically-integrated moist static energy, excluding  
207 the imposed drying  $F_q$ . This quantity becomes equal to and then slightly less than  $F_q$  only at the  
208 very largest values of the latter imposed in the lower layer. Thus the total diabatic forcing of  
209 vertically-integrated moist static energy (including  $F_q$ ) is positive for all but those experiments  
210 with the strongest drying.

211 It is of interest to compare our Figure 1 to Figure 3 in SB09, to note similarities and  
212 differences between the response to drying in our CRM and that in the SCMs used by those  
213 authors. First, the  $P-F_q$  relationship was found by SB09 to be more or less linear in the GEOS  
214 SCM as  $F_q$  is varied from 0-80 W/m<sup>2</sup>. In the MIT SCM, the effect of drying was significant for  
215  $F_q$  less than 20 W/m<sup>2</sup>, and leveled off at large drying in several cases. In our model, the reduction  
216 of precipitation occurs for  $F_q$  from 0 to greater 150 W/ m<sup>2</sup> and shows a remarkably linear  
217 relationship with  $F_q$  for lower and middle layer drying. Second, in both the SCMs in SB09,  
218 injection of dry air in the middle troposphere is more effective at suppressing precipitation,  
219 opposite to the present study. Finally, injection of dry air in the upper troposphere has different  
220 impacts in the two SCMs in SB09: the GEOS SCM shows little sensitivity, while in the MIT  
221 SCM drying in the upper troposphere is most effective at suppressing precipitation. Thus our  
222 model is more in line with the GEOS model than with the MIT model in this respect as well as

223 the linearity of the  $P$ - $F_q$  relationship, but is inconsistent with both on the relative importance of  
224 lower- vs. middle-tropospheric drying.

225 Figure 2 shows energy removal due to imposed drying,  $F_q$ , versus drying time scale  $\tau_q$ .  
226 Consistent with SB09, the two quantities are compactly related, with a nearly constant slope in  
227 the log-log plot for all the three cases.

### 228 **3.2 Large scale vertical velocity**

229 Figure 3 shows the large scale WTG vertical motion versus energy export  $F_q$ . For small  
230  $F_q$ ,  $W_{wtg}$  is top-heavy in all experiments, peaking near 250 hPa. As  $F_q$  increases, the peak value  
231 decreases and the profile becomes less top-heavy. When  $F_q$  exceeds 145 W/m<sup>2</sup> for lower layer  
232 drying,  $W_{wtg}$  becomes bottom-heavy with a peak at ~875 hPa. This bottom-heaviness does not  
233 occur even at the maximum values of upper- or middle-tropospheric drying (though those are not  
234 as large as the maximum lower-tropospheric drying), but the reduction of  $W_{wtg}$  is still clearly  
235 seen in the upper troposphere. Convective mass fluxes (not shown) vary consistently with the  
236 variation in  $W_{wtg}$ , being reduced in the upper troposphere as  $W_{wtg}$  becomes less top-heavy.

237 Figure 4 illustrates the time evolution of  $W_{wtg}$  versus height in lower layer drying for two  
238 different drying time scales,  $\tau_q=3$  and 10 days, associated with energy export  $F_q = 153$  and 52  
239 W/m<sup>2</sup>. These two cases represent two distinct regimes: 1) at  $\tau_q = 3$  d, intermittent ascent and  
240 descent are both seen at upper levels, while steady ascent is seen at lower levels. The time-  
241 averaged  $W_{wtg}$  is bottom heavy. 2) At  $\tau_q=10$  d, there is only steady ascent; there is no peak  
242 detectable at lower levels, indicating that the low level peak emerges because of imposed drying.

243 Variations of the WTG vertical motion may be further quantified by examining its  
 244 projection onto discrete vertical basis functions [Fulton and Shubert, 1985]. Here we simply  
 245 chose the basis functions as  $\sin(m\pi \frac{z}{H_0})$ , where  $H_0 = 14$  km, and  $m$  is 1 or 2. This choice is  
 246 different from that of Tulich *et al.* [2007], who performed vertical mode analysis on resolved  
 247 cloud scale vertical motions. With our chosen basis functions, projection of WTG vertical  
 248 motion  $W_m$  for the  $m$ -th mode is computed as

$$249 \quad W_m = \int_0^{H_0} W_{\text{wtg}} \sin(m\pi \frac{z}{H_0}) dz / H_0 \quad (3).$$

250 In our implementation of WTG, temperature perturbations are related to WTG vertical  
 251 motions by relaxing temperature perturbations to zero. The coupling between temperature  
 252 anomalies and WTG vertical motion occurs on the WTG time scale, which is the same for all  
 253 modes. Under the implementation of WTG used by Kuang [2008, 2011] and Blossey *et al.*  
 254 [2009], the coupling varies with the wave speed of each mode. We may expect some difference  
 255 in these two different approaches.

256 The imposed drying reduces the amplitude of both the first and second modes. This is  
 257 illustrated in Figure 5 a, which shows  $W_1$  and  $-W_2$  versus  $F_q$ . With  $F_q$  less than  $50 \text{ W/m}^2$ , drying  
 258 causes more reduction in  $W_1$  for lower layer drying than for upper layer drying, while middle  
 259 layer drying appears to fall in between, much like variations of precipitation in Figure 1. Drying  
 260 also causes reduction of  $-W_2$  in all cases, but unlike for  $W_1$ , lower layer drying does not cause  
 261 more reduction than middle and upper layer drying. For lower layer drying, both  $W_1$  and  $-W_2$   
 262 become close to zero or even negative for  $F_q \sim 150 \text{ W/m}^2$ .

263 The degree of top-heaviness may be further quantified by the ratio  $-W_2/W_1$ , similar to  
264 *Kuang* [2011]. Without drying, the ratio is  $\sim 0.9$ . Figure 5 b shows that the ratio remains nearly  
265 constant with  $F_q$  less than  $100 \text{ W/m}^2$  for lower layer drying, but decreases to  $\sim 0.7$  with  $F_q \sim 50$   
266  $\text{W/m}^2$  for upper layer drying. Thus drying in the upper layer leads to the most reduction in top-  
267 heaviness for the same net energy removal, although it has the least impact on rainfall. This is  
268 explained in terms of the moist static energy budget below, in section 3.5. For lower layer  
269 drying, the ratio  $-W_2/W_1$  eventually shows a sharp decrease to values close to zero, indicating  
270 bottom-heavy WTG vertical motions. Note that the numerical estimate of the ratio becomes  
271 problematic when  $W_1$  approaches zero, as happens for the largest values of  $F_q$  applied in the  
272 lower layer.

### 273 **3.3 Vertical profiles of thermodynamic variables**

274 Figure 6 illustrates vertical profiles of anomalous temperature, water vapor mixing ratio,  
275 and moist static energy for the three sets of experiments. (For easy comparison, the dark curves  
276 in Figure 6 indicate convective responses with similar  $F_q \sim 45 \text{ W/m}^2$ ). In all three variables, as  
277 the drying strength increases, convective responses increase as well. Convective responses are  
278 not limited to the vertical layer in which forcing is imposed. Negative temperature anomalies are  
279 found within a deep layer above the imposed forcing, while positive temperature anomalies are  
280 found below the forcing layer (Figure 6 a, d and g). The node of this dipole structure in the  
281 temperature anomalies is located at  $\sim 1 \text{ km}$  for lower layer drying,  $\sim 3 \text{ km}$  for middle layer drying,  
282 and  $\sim 6 \text{ km}$  for upper layer drying. Moisture shows the largest reduction in the layer of imposed  
283 drying, but there is also significant drying aloft and moistening within the boundary layer.  
284 Variations of MSE are combinations of temperature and moisture. MSE decreases in the free  
285 troposphere and increases within the boundary layer with strengthened drying. Reduction in

286 MSE in the free troposphere is mostly due to moisture reduction; consistent with this, the peak  
287 moisture reduction corresponds in the vertical to the peak of variations of MSE in all cases.

288         The nonlocal impact of the imposed drying on temperature and moisture is in line with  
289 other CRM studies. *Tulich and Mapes [2010]* and *Kuang [2010]* showed that positive humidity  
290 perturbations in the free troposphere cause warming at and above the layer in question, and that  
291 convection tends to counteract the humidity anomalies by cooling and drying that layer and the  
292 subcloud layer. These two studies also showed stronger sensitivities of deep convection to lower  
293 free-tropospheric perturbations than to upper tropospheric ones. *Tulich and Mapes [2010]*  
294 suggested that the strong sensitivity to lower tropospheric anomalies was a consequence of the  
295 marginal buoyancy maintained in the deep lower tropospheric layer extending from surface to 4  
296 km. Nevertheless, comparison between our results and those of *Tulich and Mapes [2010]* and  
297 *Kuang [2010]* is not entirely straightforward, because those two studies focused on the responses  
298 to temperature and moisture anomalies imposed at a specific time with no forcing thereafter,  
299 while we are interested in the statistically steady response to sustained forcing.

300         The positive anomalies of MSE and temperature within the boundary layer may indicate  
301 weakened downdrafts. Supporting evidence comes from the consideration of the energy budget  
302 of the boundary layer. The primary terms in the budget are surface fluxes and the energy fluxes  
303 associated with updrafts and downdrafts at the top of the boundary layer. Because surface fluxes  
304 decrease with drying, the increase of MSE within boundary layer can only be attributed to less  
305 energy loss at the top of the boundary layer, which is likely due to weaker downdrafts.

### 306 **3.4 Precipitation - relative humidity relation**

307         Observational studies [e.g., *Bretherton et al., 2004; Peters and Neelin, 2006; Neelin et al.,*  
308 *2009; Holloway and Neelin, 2009]* have examined the statistical relationship between

309 precipitation and column-integrated relative humidity (CRH, the column-integrated water vapor  
310 divided by its saturation value) at daily and monthly time scales. Implications of these  
311 relationships have been examined in theoretical and modeling studies [e.g., *Raymond, 2000*;  
312 *Raymond and Zeng, 2005*; *Sobel and Bellon, 2009*; *Muller et al., 2009*]. Here we examine this  
313 relationship in our experiments during the transition period from RCE to the new WTG  
314 equilibrium under both imposed drying and high SST forcings. We sample the first 10 days of all  
315 experiments after the higher SST, WTG, and drying are all switched on, corresponding to a  
316 transition period from RCE to the new equilibrium achieved under both higher SST and drying.

317 Figure 7 illustrates daily precipitation versus CRH for the three sets of experiments. In all  
318 experiments, CRH remains greater than 0.6 and below 0.8. Over this narrow range, neither  
319 quantity varies much for upper layer drying. For lower layer drying,  $P$  varies over a large range  
320 from 5 – 20 mm/d (Fig. 1) while CRH varies from 0.6-0.8. For middle layer drying, the same  $P$   
321 is associated with lower CRH and the apparent slope of the  $P$ -CRH relationship is also less,  
322 compared to lower layer drying. There is little overlap between the two sets of points.  
323 Apparently the  $P$ -CRH relationship is not universal even within this single model, but depends to  
324 some extent on the particular large-scale forcings with which convection is interacting.

325 The GEOS SCM in SB09 (their Figure 8) seems to have a similar  $P$ -CRH relationship to  
326 that in our study. In particular, the ranges of CRH (0.6-0.8) and  $P$  (5-25 mm/d) in this model are  
327 both very close to our results. However, these two variables in the MIT SCM in SB09 vary over  
328 different ranges, with CRH in particular varying between 0.4-0.6. In this respect as well, the  
329 GEOS SCM behaves more similarly to our CRM results than does the MIT SCM.

330

331 **3.5 Moist static energy budget**

332 The gross moist stability is a critical parameter in thermodynamic theories relating  
 333 precipitation to tropical large scale circulations, but remains under-constrained by either  
 334 observations or numerical modeling. It has often been assumed to be a small positive constant  
 335 [e.g., *Neelin and Held* 1987]. Recent observational studies [*López Carrillo and Raymond*, 2005,  
 336 see their Fig. 4; *Back and Bretherton*, 2006] and numerical simulations [e.g., *Bretherton et al.*  
 337 2005; *Raymond and Fuchs*, 2009; *Raymond et al.*, 2009], on the other hand, have found that it  
 338 can assume negative values.

339 The budgets of vertically integrated moist static energy ( $h$ ) and dry static energy ( $s$ ) in the  
 340 statically steady state can be written as

341 
$$\langle W_{\text{wtg}} \frac{\partial s}{\partial z} \rangle = H + P + \langle Q_R \rangle \quad \text{and} \quad \langle W_{\text{wtg}} \frac{\partial h}{\partial z} \rangle = E + H + \langle Q_R \rangle - F_q \quad (4),$$

342 where  $P$ ,  $H$ ,  $E$ , and  $Q_R$  denote precipitation, surface sensible flux, latent flux and radiative  
 343 heating, respectively.  $\langle \rangle = \int_{p_0}^{p_T} \rho dz$  denotes the mass-weighted vertical integral from the bottom  
 344 to the top of the computational domain, where  $\rho$  is density. Substituting and rearranging terms  
 345 yields the following diagnostic relation [*Sobel*, 2007],

346 
$$P = \frac{1}{M_N} (E + H + \langle Q_R \rangle - F_q) - \langle Q_R \rangle - H \quad (5),$$

347 where we have defined  $M_N$ , the normalized gross moist stability:

348 
$$M_N = \langle W_{\text{wtg}} \frac{\partial h}{\partial z} \rangle / \langle W_{\text{wtg}} \frac{\partial s}{\partial z} \rangle \quad (6).$$

349 This is essentially identical to the “gross moist stability ratio” used in *Sobel and Bellon* [2009],  
 350 with the only difference that the latter was computed in pressure coordinates. We denote the

351 nominator and denominator as  $A_h$  and  $A_s$ , which represent the vertically-integrated vertical  
352 advection of moist and dry static energy, respectively, by the WTG vertical velocity. A relation  
353 similar to but slightly different from (5) is obtained if moisture convergence is used instead of  
354 vertical advection of dry static energy as the normalization factor in the definition of  $M_N$  [e.g.,  
355 *Raymond et al.*, 2009]. To estimate  $M_N$ , we sample the model data every 12 hours, then compute  
356 the time and domain averages of  $A_h$  and  $A_s$ , separately, and finally divide them. Our simple  
357 radiative scheme produces nearly constant vertically-integrated radiative cooling of  $\sim 145 \text{ W/m}^2$   
358 (it can vary by  $\sim 1 \text{ W/m}^2$ ). The surface fluxes increase slowly and roughly linearly with drying  $F_q$ ,  
359 as shown in Figure 1b.

360 Figure 8 a shows  $M_N$  versus the energy export  $F_q$  in all the cases.  $M_N$  remains positive for  
361 most experiments, except for a few with large drying imposed in the lower layer. The slope of  
362 the relationship between  $M_N$  and  $F_q$  is different in the three cases. For upper layer drying,  $M_N$   
363 decreases over the small range (0.3-0.15) when  $F_q$  is less than  $50 \text{ W/m}^2$ . For middle layer drying,  
364  $M_N$  remains constant for  $F_q < 50 \text{ W/m}^2$ , then gradually decreases for  $F_q > 80 \text{ W/m}^2$ , but  
365 remains positive ( $\sim 0.15$ ). For lower layer drying,  $M_N$  is nearly invariant when  $F_q < 100 \text{ W/m}^2$ ,  
366 and then turns negative sharply at the largest values of  $F_q$  where the total moist static energy  
367 forcing (including  $F_q$ ) becomes negative (see Fig. 1b and accompanying discussion in section  
368 3.1).

369 The normalized gross moist stability  $M_N$  can vary due to either vertical advection of  
370 moist static energy,  $A_h$ , or vertical advection of dry static energy,  $A_s$ . We first consider  $A_h$ .  
371 Equation (4) indicates that vertical advection of moist static energy need not be simply related to  
372 precipitation. However, equation (4) and Figure 1b together show that the energy removal due to  
373 drying,  $F_q$ , is mostly balanced by vertical advection, because variations in surface fluxes (Figure

374 1b) and radiation are both very small compared to those in  $F_q$ . Hence,  $A_h$  varies similarly with  
375 respect to  $F_q$  for all three cases, as illustrated in Figure 8 b. However,  $A_s$  must co-vary with  
376 precipitation, as can be deduced from the dry static energy equation (4). Figure 8 b also shows  
377 that  $A_s$  has slopes very similar to those in the  $P$ - $F_q$  relation in Figure 1 b. Therefore, variations in  
378  $M_N$  are mainly related to  $A_s$ , but not to  $A_h$ , which varies similarly for drying at different layers.

379 Variations of  $A_h$  and  $A_s$  can also be illustrated in the phase space in Figure 8 c.  $M_N$   
380 corresponds to the ratio  $A_h/A_s$ . The ratio is relatively constant for large  $A_h$  or  $A_s$ . In the lower  
381 layer drying experiments, when  $F_q$  falls between 140 and 160  $\text{W/m}^2$ ,  $A_s$  is reduced to values  
382 close to zero and variations in  $M_N$  become large, while the total MSE forcing  $E+H+\langle Q_R \rangle - F_q$   
383 becomes small and then changes sign.

384 Figure 8 can be compared to Figure 10 of SB09.  $M_N$  estimated in SB09 varies over large  
385 ranges in the two SCMs. The overall reduction of  $M_N$  in our model is broadly consistent with that  
386 in the GEOS model. That model also shows negative  $M_N$  in response to sufficiently strong  
387 drying in the lower layer; the negative values occurred for  $F_q$  greater than about 70  $\text{W/m}^2$ , about  
388 half that required to cause negative  $M_N$  in our results. On the other hand,  $M_N$  in the MIT SCM  
389 increases with respect to drying.

390 The accuracy of the computation of  $M_N$  can be quantified by comparing the estimated  $P$   
391 using equation (5) against the directly simulated  $P$ . Figure 9 shows that the budget-derived  
392 estimates of  $P$  (thick symbols) compare well with directly simulated values. The steadiness  
393 assumed by equation (5) is not strictly satisfied, but the small deviations of estimated  $P$  from the  
394 directly simulated values suggest that transients have only a minor effect in these integrations.

395 The constancy of  $M_N$  for integrations with lower-tropospheric drying over most of the  
396 range of  $F_q$  suggests a particularly simple interpretation of that case. The dashed gray line in

397 Figure 1b shows the quantity  $P_0 - F_q / M_{N0}$  where  $P_0$  and  $M_{N0}$  are the values of  $P$  and  $M_N$  when  $F_q$   
398 = 0. From equation (5), this is the precipitation which would occur if neither surface fluxes nor  
399 the normalized gross moist stability  $M_N$  varied from their values in the absence of imposed  
400 drying (recall that radiative cooling is constrained to be nearly constant). The precipitation  
401 variations would then simply be equal to the imposed drying magnified by the inverse of the  
402 constant normalized gross moist stability. Since the latter and the unperturbed surface fluxes are  
403 known from the solution with no drying, this could be viewed as a predictive perturbation theory  
404 for the response of precipitation to drying, given the unperturbed solution. The figure shows that  
405 the resulting estimate is remarkably accurate. (In fact it is fairly accurate even for large  $F_q$ ,  
406 where  $M_N$  is not at all constant; the agreement is apparently accidental.) For drying in the middle  
407 troposphere,  $M_N$  decreases with  $F_q$  while the quantity in parentheses in (5) – the primary variable  
408 part of the forcing – remains positive; decrease in that quantity due to increasing  $F_q$  is partially  
409 compensated by decreasing  $M_N$ , leading to a muted response in precipitation compared to the  
410 lower-tropospheric drying case. For upper-tropospheric drying, the compensation is almost  
411 perfect so that  $P$  remains nearly constant.

412         These results illustrate some of the subtleties inherent in constructing theories based on  
413 the vertically integrated moist static energy budget. For our integrations with lower-tropospheric  
414 drying, that budget appears to offer a useful interpretation. Because the normalized gross moist  
415 stability stays nearly constant, a simple perturbation theory can explain the response to imposed  
416 drying given only information about the unperturbed case. For upper-tropospheric drying, the  
417 opposite is true. The result (constant precipitation) can be stated very simply. Yet its explanation  
418 in terms of the moist static energy budget is more complex, involving cancellation of the  
419 imposed drying by changes in the normalized gross moist stability, which in turn result from

420 changes in vertical structure as shown in Figure 5. The case of middle-tropospheric drying lies  
421 between these two extremes. It is not clear to us how one could have anticipated this varied  
422 behavior before performing and analyzing the model integrations.

#### 423 **4. Discussion and conclusions**

424 We have explored the response of convection to imposed drying using a cloud-resolving  
425 model under the weak temperature gradient approximation. The drying is imposed in three layers  
426 – in the lower, middle and upper free troposphere – in three sets of model integrations, to mimic  
427 advection of dry air into rainy regions in these distinct layers. Design of our numerical  
428 experiments closely follows *Sobel and Bellon* [2009]. The main findings can be summarized  
429 below.

430 Daily rain rates decrease with drying when the drying is imposed in the lower or middle  
431 free troposphere. The decrease in precipitation is quite linear with respect to drying, even when  
432 the energy export by drying reaches  $150 \text{ W/m}^2$ . Drying in the lower free troposphere is most  
433 effective in suppressing convection and reducing rainfall, while drying in the upper troposphere  
434 has little impact, and drying at middle layers falls in between. The linear slope of precipitation  
435 versus energy export associated with drying is 3.1, 1.9, and -0.4 for drying imposed for lower,  
436 middle and upper tropospheric drying, respectively. For lower tropospheric drying, this slope is  
437 very close to the inverse of the normalized gross moist stability, which remains approximately  
438 constant over much of the range in drying strength and thus can be computed from the  
439 unperturbed case with no drying.

440 The parameterized large scale vertical motion is top-heavy over a large range of drying,  
441 but its vertical structure responds differently to drying at different levels. While the amplitude of

442 large-scale vertical motion, like precipitation, responds most strongly to lower tropospheric  
443 drying and least to upper tropospheric drying, the opposite is true of the shape of the large-scale  
444 vertical motion profile and normalized gross moist stability. The vertical motion profile  
445 becomes less top-heavy as upper tropospheric drying increases; this decreases the normalized  
446 gross moist stability, allowing precipitation to stay nearly constant despite the imposed drying.  
447 For lower-tropospheric drying, the shape of the vertical motion profile and value of the  
448 normalized gross moist stability remain roughly constant as drying increases over most of its  
449 range, allowing a strong decrease in precipitation. For the largest values of lower tropospheric  
450 drying, however, the vertical motion profile becomes bottom-heavy and the normalized gross  
451 moist stability becomes negative. A parsimonious explanation of all these results would appear  
452 to be a challenging target for any simple theory based on the vertically-integrated moist static  
453 energy budget.

#### 454 **Acknowledgements**

455 This work was supported by NSF grant AGS-1008847. We also thank NCAR's computational  
456 and Information Systems Laboratory, where initial tests of our model were performed.

## Reference

- 457 Allen, G., Vaughan, G., Brunner, D., T. May, P., Heyes, W., Minnis, P. and K. Ayers, J. (2009),  
458 Modulation of tropical convection by breaking Rossby waves. *Quart. J. Roy. Meteor. Soc.*,  
459 135: 125–137. doi: 10.1002/qj.349
- 460 Back, L. E., and C. S. Bretherton (2006), Geographic variability in the export of moist static  
461 energy and vertical motion profiles in the tropical Pacific. *Geophys. Res. Lett.*, 33, L17810,  
462 doi:10.1029/2006GL026672.
- 463 Blossey, P. N., C. S. Bretherton, and M. C. Wyant (2009), Understanding subtropical low cloud  
464 response to a warmer climate in a superparameterized climate model. Part II: Column modeling  
465 with a cloud-resolving model. *J. Adv. Model Earth Syst.*, 1, 14 pp.,  
466 doi:10.3894/JAMES.2009.1.8 .
- 467 Bretherton, C. S., P. N. Blossey, and M. Khairoutdinov (2005), An energy-balance analysis of  
468 deep convective self-aggregation above uniform SST. *J. Atmos. Sci.*, 62, 4273–4292
- 469 Bretherton, C. S., M. E. Peters, and L. E. Back (2004), Relationships between Water Vapor Path  
470 and Precipitation over the Tropical Oceans. *J. Clim.*, 17, 1517-1528
- 471 Brown, R. G., and C. Zhang (1997), Variability of midtropospheric moisture and its effect on  
472 cloud-top height distribution during TOGA COARE. *J. Atmos. Sci.*, 54, 2760–2774.
- 473 Derbyshire, S. H., I. Beau, P. Bechtold, J.-Y. Grandpeix, J.-M. Piriou, J.-L. Redelsperger, and P.  
474 M. Soares (2004), Sensitivity of moist convection to environmental humidity. *Quart. J. Roy.*  
475 *Meteor. Soc.*, 130, 3055–3080.
- 476 Frierson, D. M. W. (2007), The dynamics of idealized convection schemes and their effect on the  
477 zonally averaged tropical circulation. *J. Atmos. Sci.*, 64, 1959-1976.
- 478 Frierson, D. M. W., D. Kim, I.-S. Kang, M. Lee, and J.-I. Lin (2011), Structure of AGCM-  
479 simulated convectively coupled equatorial waves and sensitivity to convective parameterization.  
480 *J. Atmos. Sic.*, 68, 26-45.
- 481 Fulton, S. R., and W. H. Schubert (1985), Vertical normal transforms: Theory and application.  
482 *Mon. Wea. Rev.*, 113, 647–658.
- 483 Holloway, C. H., and J. D. Neelin (2009), Moisture vertical structure, column water vapor, and  
484 tropical deep convection. *J. Atmos. Sci.*, 66, 1665–1683.
- 485 James, R. P., and P. M. Markowski (2010), A numerical investigation of the effects of dry air  
486 aloft on deep convection. *Mon. Wea. Rev.*, 138, 140–161.
- 487 Klemp, J. B., J. Dudhia, and A. Hassiotis (2008), An upper gravity wave absorbing layer for  
488 NWP applications. *Mon. Wea. Rev.*, 136, 3987–4004.
- 489 Kuang, Z. (2008), Modeling the interaction between cumulus convection and linear waves using  
490 a limited domain cloud system resolving model, *J. Atmos. Sci.*, 65, 576-591.
- 491 Kuang, Z. (2010), Linear response functions of a cumulus ensemble to temperature and moisture  
492 perturbations and implication to the dynamics of convectively coupled waves, *J. Atmos. Sci.*, 67,  
493 941-962

494 Kuang, Z. (2011), The wavelength dependence of the gross moist stability and the scale selection  
495 in the instability of column integrated moist static energy, *J. Atmos. Sci.*, *68*, 61-74.

496 Lindzen, R. S., and S. Nigam (1987), On the role of sea surface temperature gradients in forcing  
497 low-level winds and convergence in the tropics. *J. Atmos. Sci.*, *44*, 2418-2436.

498 López Carrillo, C., and D. J. Raymond (2005), Moisture tendency equations in a tropical  
499 atmosphere. *J. Atmos. Sci.*, *62*, 1601–1613.

500 Lucas, C., and E. J. Zipser (2000), Environmental variability during TOGA COARE. *J. Atmos.*  
501 *Sci.*, *57*, 2333-2350.

502 Mapes, B. E. (2004), Sensitivities of cumulus ensemble rainfall in a cloud-resolving model with  
503 parameterized large-scale dynamics. *J. Atmos. Sci.*, *61*, 2308–2317.

504 Muller, C. J., L. E. Back, P. A. O’Gorman, and K. A. Emanuel (2009), A model for the  
505 relationship between tropical precipitation and column water vapor. *Geophys. Res. Lett.*, *36*,  
506 L16804, doi:10.1029/2009GL039667

507 Neelin, J. D. (1997), Implications of convective quasi-equilibria for the large-scale flow. Smith,  
508 R. K. (Ed.) *The Physics and Parameterization of Moist Atmospheric Convection*, pp. 413-446,  
509 Elsevier (Amsterdam).

510 Neelin, J. D., and I. M. Held (1987), Modeling tropical convergence based on the moist static  
511 energy budget. *Mon. Weather Rev.*, *115*, 3-12.

512 Nolan, D. S., C. Zhang, and S. Chen (2007), Dynamics of the shallow circulation around ITCZ  
513 regions. *J. Atmos. Sci.*, *64*, 2262-2285

514 Neelin, J. D., O. Peters, J. W.-B. Lin, K. Hales, and C. E. Holloway (2009), Rethinking  
515 convective quasi-equilibrium: observational constraints for stochastic convective schemes in  
516 climate models In *Stochastic Physics and Climate Modelling*, T. N. Palmer and P. D. Williams,  
517 eds. Cambridge University Press, Cambridge

518 Nolan, D. S., S. W. Powell, C. Zhang, and B. E. Mapes (2010), Idealized simulations of the  
519 ITCZ and its multi-level flows. *J. Atmos. Sci.*, *67*, 4028-4053.

520 Peters, M. E., Z. Kuang, and C. C. Walker (2008), Analysis of Atmospheric Energy Transport in  
521 ERA-40 and Implications for Simple Models of the Mean Tropical Circulation. *J. Climate*, *21*,  
522 5229–5241.

523 Peters, O., and J. D. Neelin (2006), Critical phenomena in atmospheric precipitation. *Nature*  
524 *Physics*, *2*, 393-396, doi:10.1038/nphys314.

525 Raymond, D. J. (2000), Thermodynamic control of tropical rainfall. *Quart. J. Roy. Meteor. Soc.*,  
526 *126*, 889–898, doi:10.1002/qj.49712656406.

527 Raymond, D. J., and X. Zeng (2005), Modelling tropical atmospheric convection in the context  
528 of the weak temperature gradient approximation. *Quart. J. Roy. Meteor. Soc.*, *131*, 1301-1320

529 Raymond, D. J., and S. L. Sessions (2007), Evolution of convection during tropical  
530 cyclogenesis. *Geophys. Res. Lett.*, *34*, L06811, doi:10.1029/2006GL028607.

531 Raymond, D. J., and Z. Fuchs (2009), Moisture modes and the Madden-Julian oscillation. *J.*  
532 *Climate*, 22, 3031-3046.

533 Raymond, D. J., S. L. Sessions, A. H. Sobel, and Z. Fuchs (2009), The mechanics of gross moist  
534 stability. *J. Adv. Model. Earth Syst.*, 1, Art. #9, 20 pp., doi:10.3894/JAMES.2009.1.9

535 Redelsperger, J. L., Parsons, D. B., and Guichard, F. (2002), Recovery processes and factors  
536 limiting cloud-top height following the arrival of a dry intrusion observed during TOGA  
537 COARE. 59, *J. Atmos. Sci.*, 2438-2457.

538 Roca, R., J. P. Lafore, C. Piriou, and J. L. Redelsperger (2005), Extratropical dry-air intrusions  
539 into the West African monsoon midtroposphere: An important factor for the convective activity  
540 over the Sahel, *J. Atmos. Sci.*, 62, 390–407.

541 Sessions, S., D. J. Raymond, and A. H. Sobel (2010), Multiple equilibria in a cloud-resolving  
542 model. *J. Geophys. Res.*, 115, D12110, doi:10.1029/2009JD013

543 Sherwood, S. C. (1999), Convective precursors and predictability in the tropical western Pacific.  
544 *Mon. Wea. Rev.*, 127, 2977–2991.

545 Sherwood, S. C., and R. Wahrlich (1999), Observed evolution of tropical deep convective events  
546 and their environment. *Mon. Wea. Rev.*, 127, 1777–1795.

547 Skamarock, W. C., J. B. Klemp, J. Dudhia, D. O. Gill, D. M. Barker, M. G. Duda, X. Huang, W.  
548 Wang, and J. G. Powers (2008), A description of the Advanced Research WRF version 3. *NCAR*  
549 *Tech. Note NCAR/TN-475+STR*, 125 pp.

550 Sobel, A. H. (2003), On the coexistence of an evaporation minimum and precipitation maximum  
551 in the warm pool. *J. Clim.*, 16, 1003-1009

552 Sobel, A. H. (2007), Simple models of ensemble-averaged tropical precipitation and surface  
553 wind, given the sea surface temperature. *The Global Circulation of the Atmosphere*, Princeton  
554 University Press, 219–251.

555 Sobel, A. H., and C. S. Bretherton (2000), Modeling tropical precipitation in a single column. *J.*  
556 *Clim.*, 13, 4378-4392

557 Sobel, A.H. and J. D. Neelin (2006), The boundary layer contribution to intertropical  
558 convergence zones in the quasi-equilibrium tropical circulation model framework. *Theoretical*  
559 *and Computational Fluid Dynamics*, 20, 323-350

560 Sobel, A. H., S. E. Yuter, C. S. Bretherton, and G. N. Kiladis (2004), Large-scale meteorology  
561 and deep convection during TRMM KWAJEX. *Mon. Wea. Rev.*, 132, 422-444

562 Sobel, A. H., and G. Bellon (2009), The effect of imposed drying on parameterized deep  
563 convection, *J. Atmos. Sci.*, 66, 2085-2096.

564 Straub, K. H., and G. N. Kiladis (2002), Observations of a convectively coupled Kelvin wave in  
565 the eastern Pacific ITCZ. *J. Atmos. Sci.*, 59, 30–53.

566 Straub, K. H., and G. N. Kiladis (2003), The observed structure of convectively coupled Kelvin  
567 waves: Comparison with simple models of coupled wave instability. *J. Atmos. Sci.*, 60, 1655–  
568 1668.

- 569 Takemi, T., O. Hirayama, and C. Liu (2004), Factors responsible for the vertical development of  
570 tropical oceanic cumulus convection, *Geophys. Res. Lett.*, *31*, L11109.
- 571 Tulich, D. A. Randall, and B. E. Mapes (2007), Vertical-mode and cloud decomposition of large-  
572 scale convectively coupled gravity waves in a two-dimensional cloud-resolving model. *J. Atmos.*  
573 *Sci.*, *64*, 1210–1229.
- 574 Tulich, Stefan N., Brian E. Mapes (2010), Transient environmental sensitivities of explicitly  
575 simulated tropical convection. *J. Atmos. Sci.*, *67*, 923–940. doi: 10.1175/2009JAS3277.1
- 576 Wang, S, and A. H. Sobel (2011), Response of convection to relative SST: cloud-resolving  
577 simulations in 2D and 3D. *J. Geophys. Res.*, *116*, D11119, 2011 doi:10.1029/2010JD015347
- 578 Webster, P. J., and R. Lukas (1992), TOGA COARE: The coupled ocean-atmosphere response  
579 experiment. *Bull. Amer. Meteor. Soc.*, *73*, 1377-1416.
- 580 Yoneyama, K., and T. Fujitani (1995), The behavior of the dry westerly air associated with  
581 convection observed during the TOGA COARE R/V Natsushima cruise. *J. Meteor. Soc. Japan*,  
582 *73*, 291–304.
- 583 Yuan, J. and D. L. Hartmann (2008), Spatial and temporal dependence of clouds and their  
584 radiative impacts on the large-scale vertical velocity profile, *J. Geophys. Res.*, *113*, D19201,  
585 doi:10.1029/2007JD009722.
- 586 Zhang, C, D. S. Nolan, C. D. Thorncroft, and H. Nguyen (2008), Shallow meridional circulations  
587 in the tropical atmosphere. *J. Clim.*, *21*, 3453-3470.
- 588 Zuidema, P., B. Mapes, J. Lin, C. Fairall and G. Wick (2006), The interaction of clouds and dry  
589 air in the eastern tropical pacific. *J. Clim.*, *19*, 4531–4544. doi: 10.1175/JCLI3836.1

**Table 1** Time scales of imposed drying for three sets of experiments

	Vertical layer of drying	Drying time scales $\tau_q$ (days)
Lower layer drying	$0.6 < \eta < 0.825$	2.9167, 2.9375, 2.9583, 2.9792, 3.0, 3.0833, 3.1667, 3.25, 3.5, 3.75, 4, 4.5, 5, 5.625, 6.25, 7.5, 8.75, 10, 12.5, 15, 20, 25, 37.5, 50, 75, 100 days
Middle layer drying	$0.375 < \eta < 0.6$	1.25, 1.375, 1.5, 1.67, 1.83, 2, 2.5, 3, 3.5, 3.92, 4, 5, 6, 10, 20, 25, 37.5, 50 days
Upper layer drying	$0.15 < \eta < 0.375$	0.25, 0.375, 0.5, 0.625, 0.75, 1, 1.5, 2, 3, 4, 6, 10, 20 days

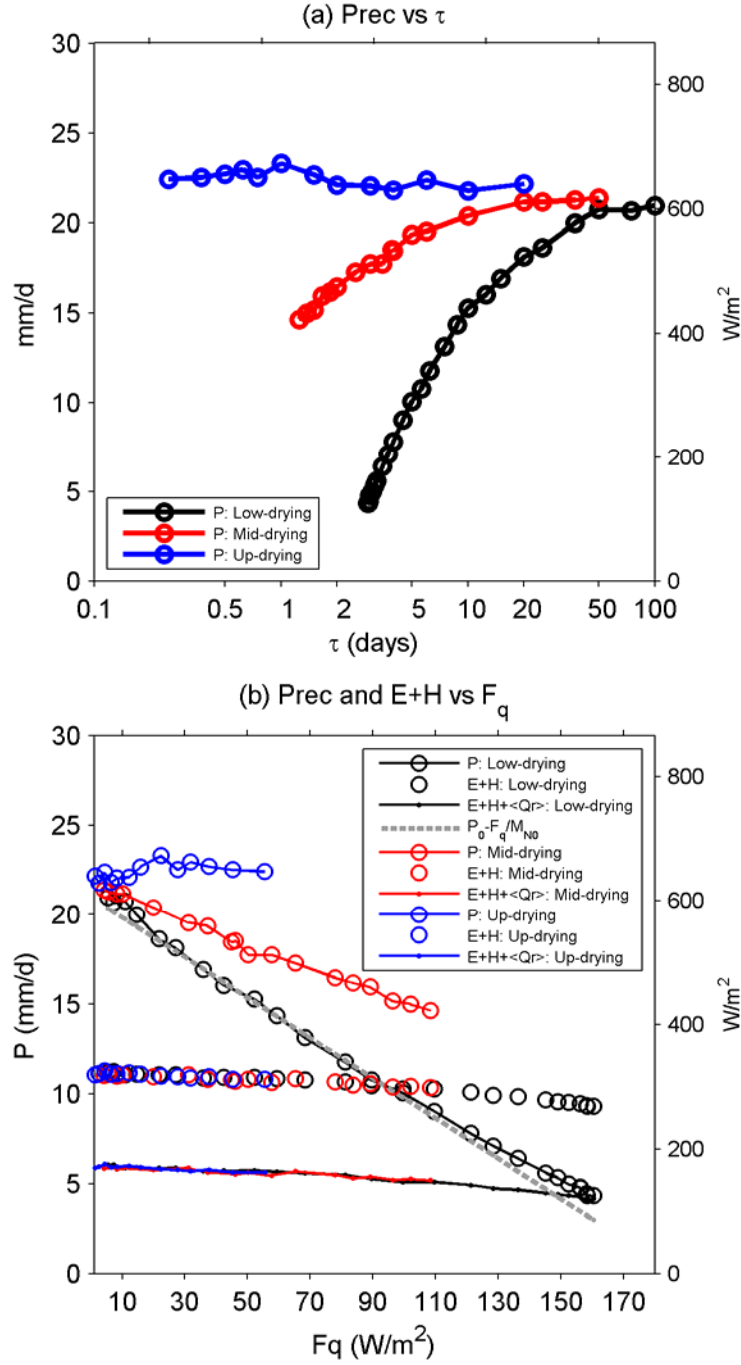


**Figure 1.** (a) Precipitation versus drying time scale  $\tau_q$ . (b) Various budget terms as a function of energy removal  $F_q$ : precipitation, surface fluxes  $E+H$ , and surface fluxes minus column-integrated radiation cooling  $E+H+\langle Q_R \rangle$ . The gray dashed line shows the quantity:  $P_0 - F_q/M_{N0}$ . See discussion in Section 3.5.

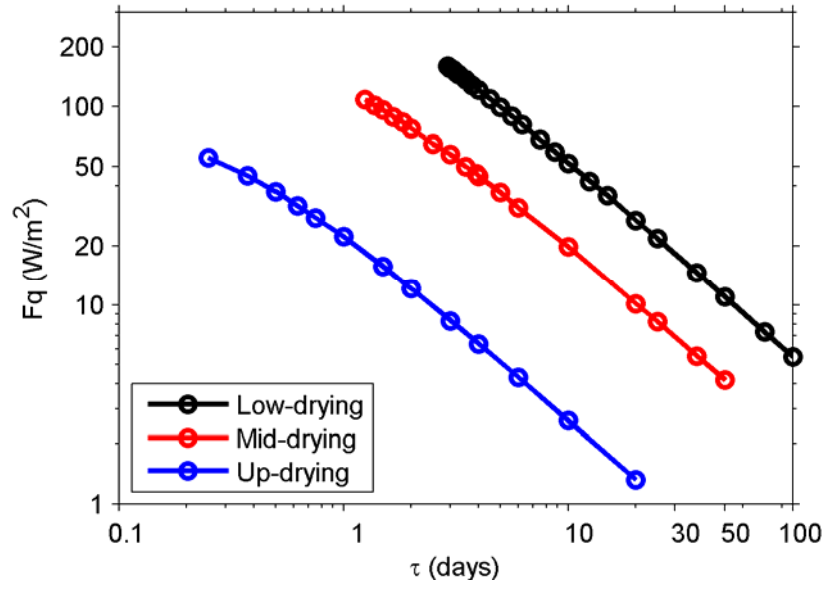


**Figure 2.** Export of moist static energy  $F_q$  versus drying time scale  $\tau_q$  on a log-log scale.

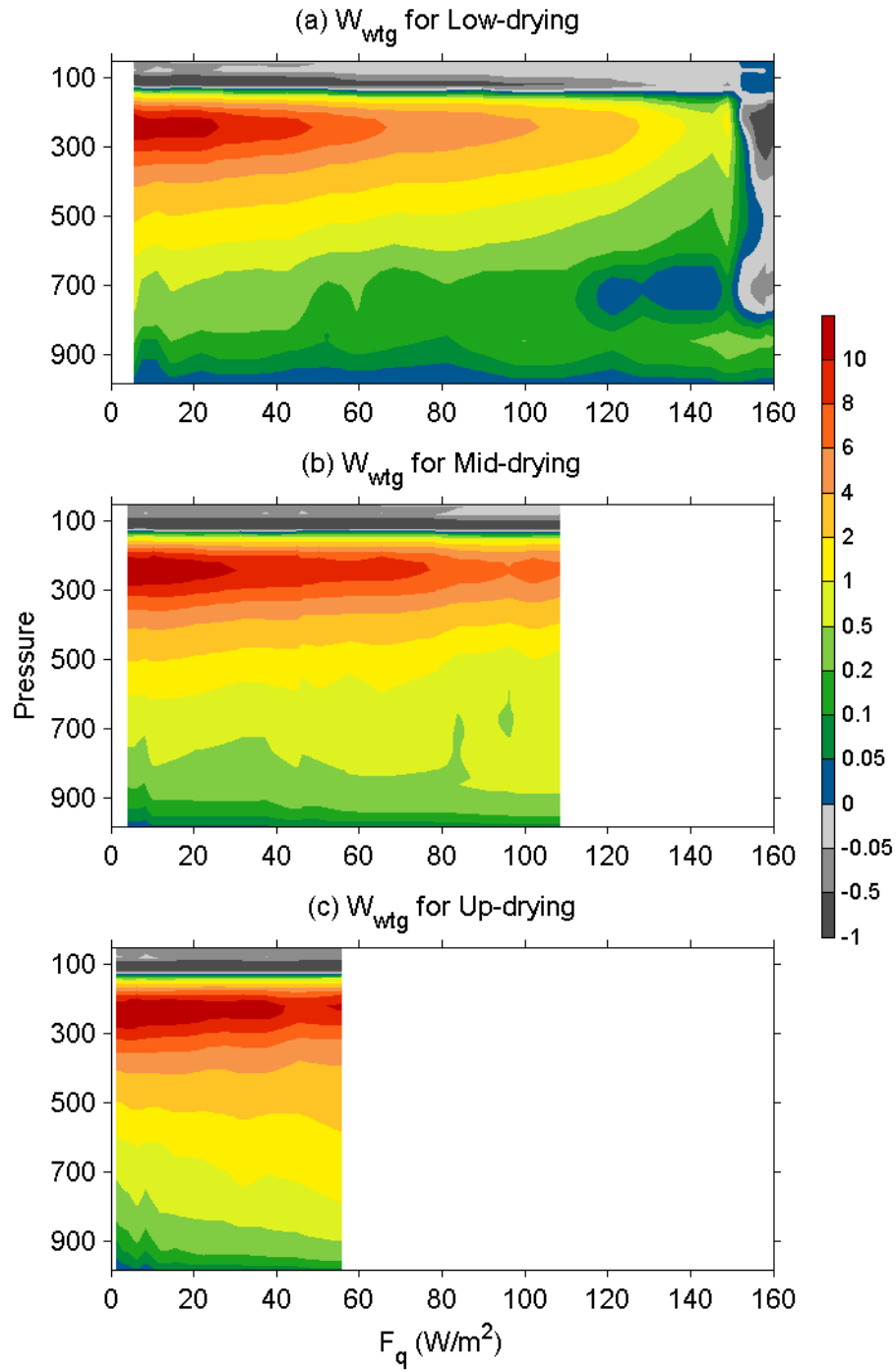


**Figure 3.** WTG vertical velocity (cm/s) for (a) lower layer drying, (b) middle layer drying, and (c) upper layer drying.

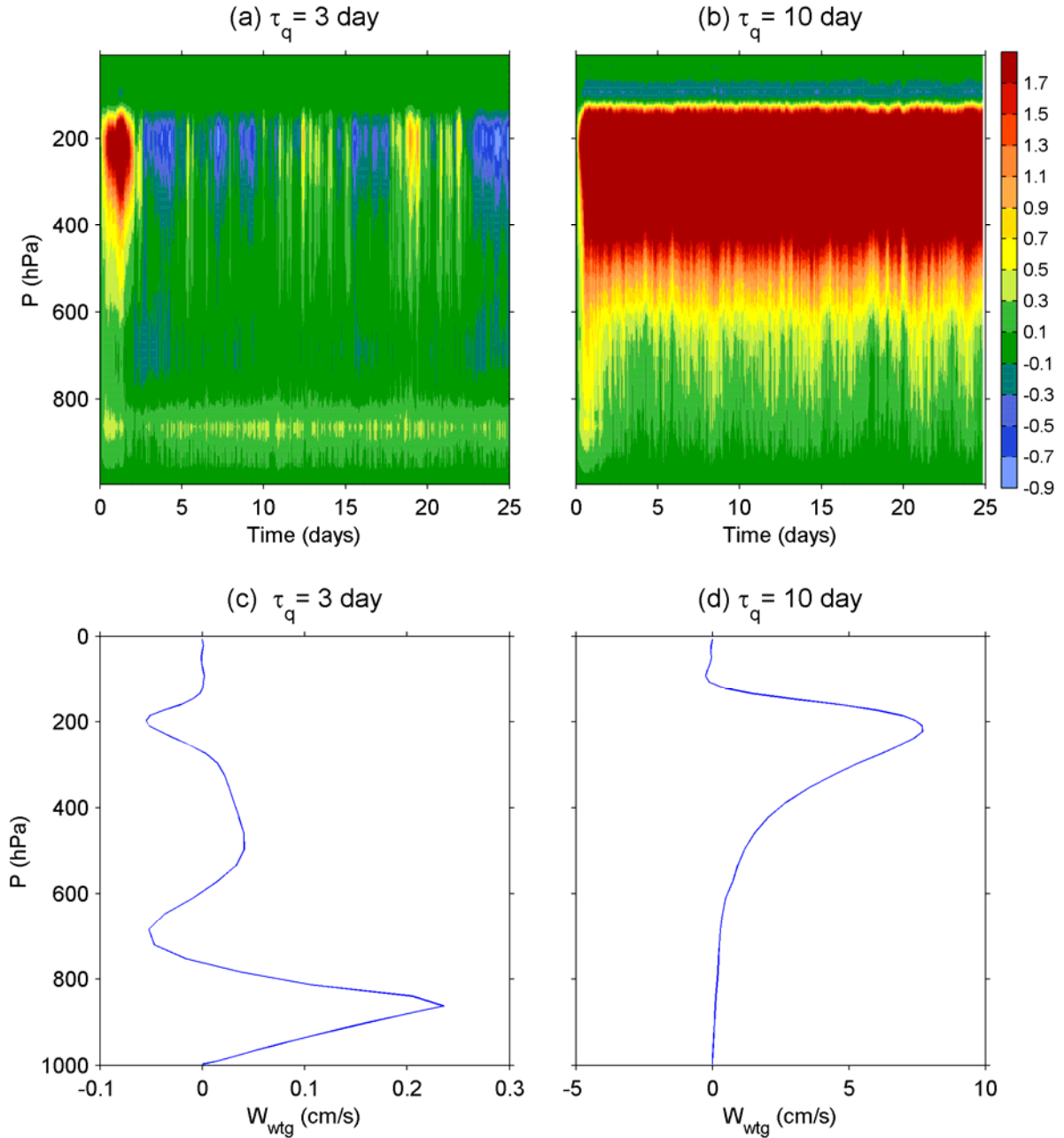


**Figure 4.** Top panels show time series of WTG vertical velocity for  $\tau_q = 3$  days in (a) and 10 days in (b) for drying at lower troposphere.  $F_q$  in these two experiments is  $156 \text{ W/m}^2$  and  $52 \text{ W/m}^2$ . Lower panels show time-averaged values of WTG vertical velocity for the two cases.

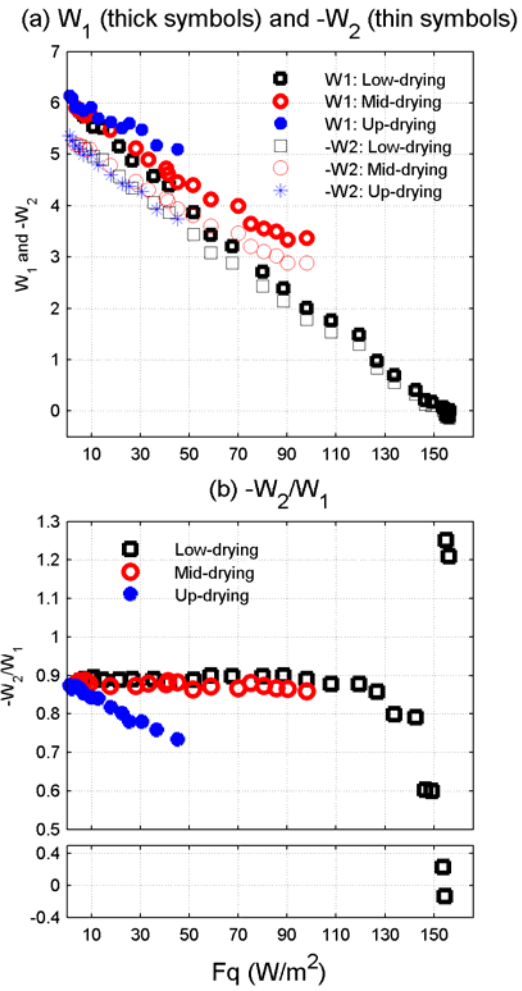


**Figure 5.** (a) Projection of  $W_{wig}$  to the 1<sup>st</sup> mode,  $W_1$  (thick symbols) and the 2<sup>nd</sup> mode,  $W_2$  ( $-W_2$ , thin symbols). (b) shows the ratio  $-W_2/W_1$ , indicating top-heaviness.

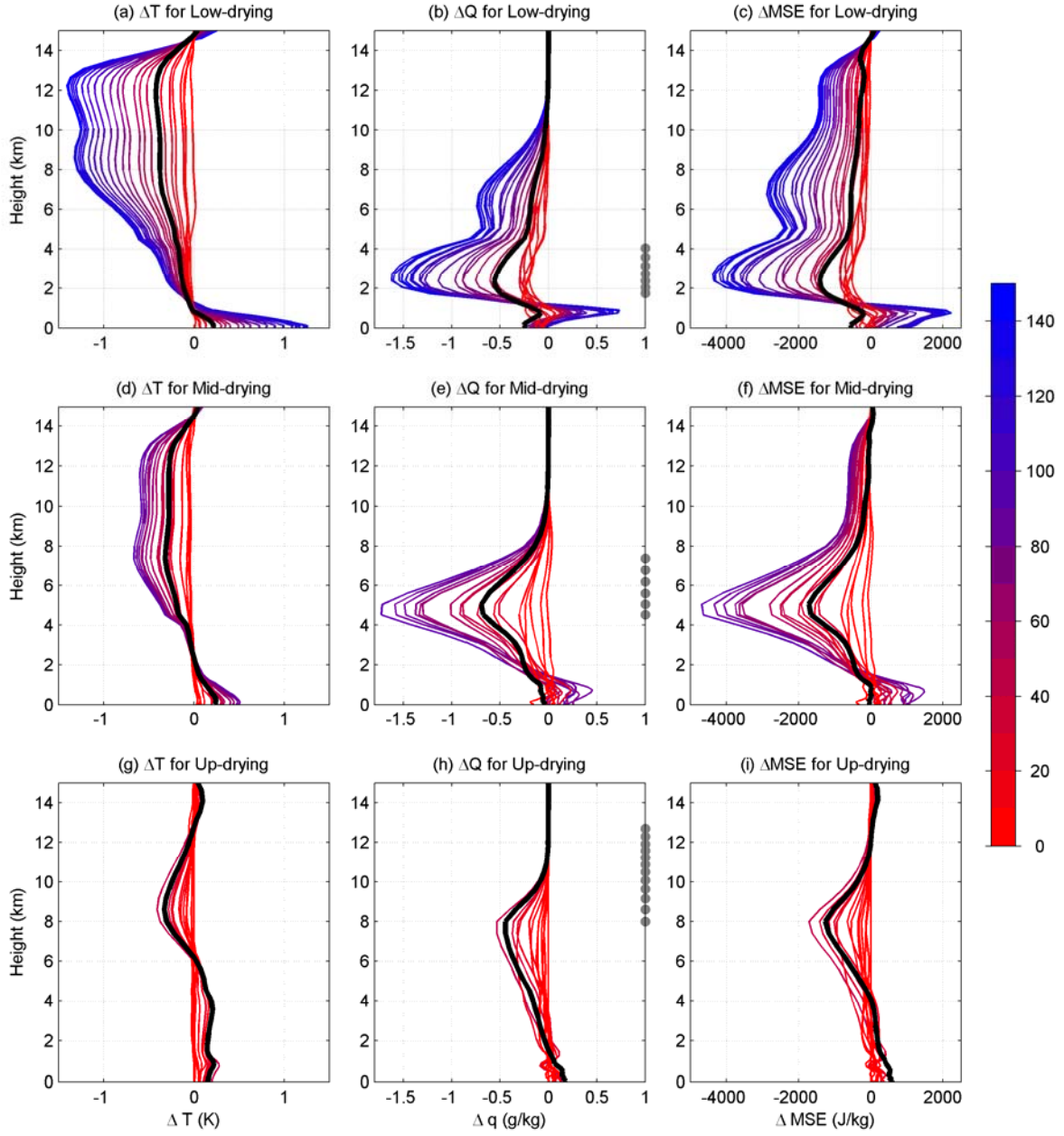


**Figure 6.** Drying induced anomalous temperature  $T$  (left column, K), water vapor mixing ratio  $Q$  (mid column, g/kg), and MSE (right column, J/kg) for lower, middle and upper drying from the top row to the bottom row. The legend of the colorbar denotes the corresponding energy export  $F_q$ . The dark curves in each panel indicate the response for  $F_q \sim 45 W/m^2$ . The gray dots in the mid-column indicate the vertical levels of the imposed drying.

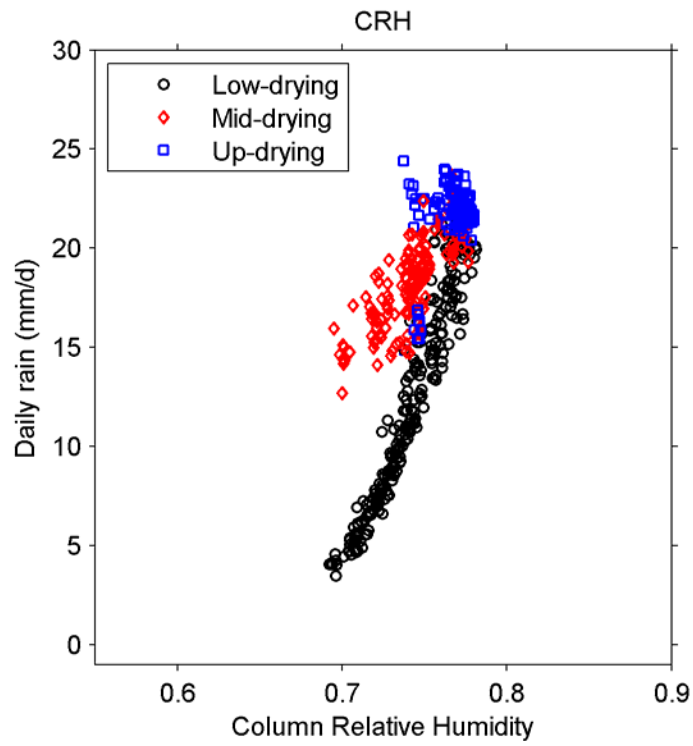


**Figure 7.** Precipitation (mm/day) versus column relative humidity (CRH) for the lower, middle and upper layer drying.

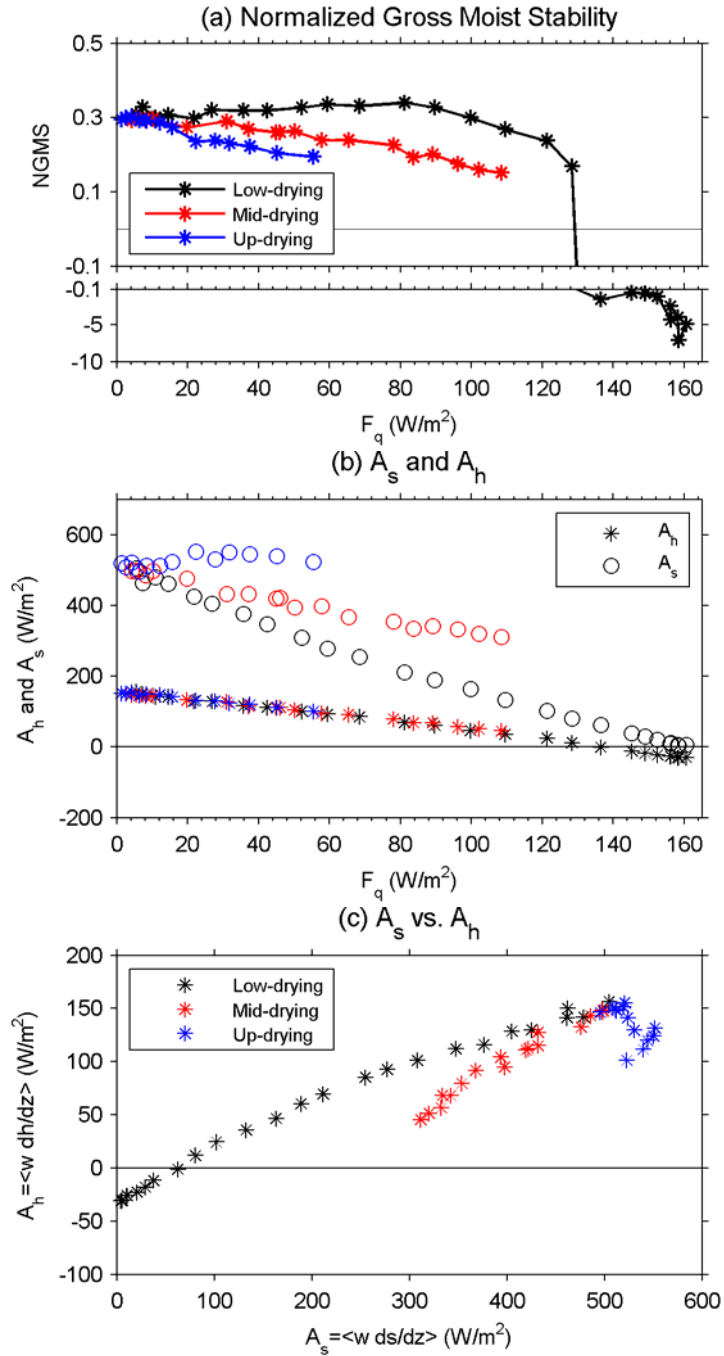


**Figure 8.** (a) Normalized gross moist stability for the lower, middle and upper layer drying. Several large values at  $F_q$  greater than  $130$   $W/m^2$  are shown in a separate scale. (b)  $A_h$  and  $A_s$  versus drying time scale  $\tau_q$ . (c)  $A_h$  versus  $A_s$ .

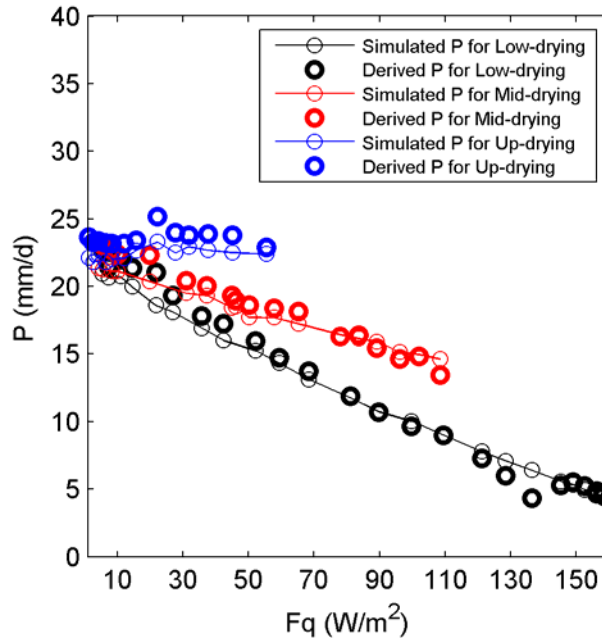


**Figure 9.** Precipitation derived from the MSE budget equation (5) (thick symbols), and directly simulated precipitation (thin symbols).